Flow Structures and Charge Behaviors of Electroconvective Silicone Flows Induced by a Surface Dielectric Barrier Injection Actuator Subjected to Bipolar Pulsed DC Signals

Zelu Yan, Christophe Louste, Philippe Traoré, Roberto Sosa

Flow Structures and Charge Behaviors of Electroconvective Silicone Flows Induced by a Surface Dielectric Barrier Injection Actuator Subjected to Bi-polar Pulsed DC Signals

Zelu Yan, *Member, IEEE*, Christophe Louste, Philippe Traoré and Roberto Sosa

***Abstract*—Surface dielectric barrier injection (SDBI) actuators have received increasing interest due to the presence of dielectric barriers, which can greatly improve the applied voltage. The success of SDBI actuators in driving silicone oil makes silicone flow a very promising application in the field of microfluidics. However, polarity-dependent flows that are different from conventional cases are observed experimentally under bi-polar pulsed DC signals. To interpret this specific phenomenon, a new model of electrohydrodynamic (EHD) wall jet considering both electrochemical injection and the initial presence of an electrical double layer (EDL) at the dielectric solid/liquid interface is developed for the first time based on the finite element method. The results show that the flow field in the simulation is consistent with the experimental bidirectional flow field. The silicone vortex movement is accompanied by charge injection, migration and accumulation in the near-wall region. Through studies of the effect of signal parameters on flow behavior, including voltage amplitude, duty cycle, frequency and waveform, a square wave signal with a frequency of 0.2 Hz proves to be the most efficient in generating a high-velocity silicone flow.**

***Index Terms*—electrohydrodynamic (EHD), surface dielectric barrier injection (SDBI), silicone oil, electrical double layer (EDL), space charge.**

I. Introduction

The electrohydrodynamic (EHD) phenomenon depends largely on actuator geometry, electrode/fluid properties and applied signals. Among all electrode configurations, the surface dielectric barrier injection (SDBI) actuator, inspired by the dielectric barrier discharge (DBD) actuator in gases, has been successfully transferred to flow control in liquids [1]. The presence of a dielectric layer permits achieving a high electric field without involving electrical breakdown. In terms of working liquids, researchers are dedicated to looking for alternatives to mineral oils for electrical equipment such as transformers. Given its good viscosity-temperature performance, low volatility and nontoxicity, silicone oil has been systematically investigated experimentally as an innovative EHD fluid [2]. In view of the mature foundation of digital microfluidics of droplets in silicone oil [3] and the progress achieved by EHD pumps on the meso- and micro-scale in recent years [4], the silicone oil-based EHD pumping technology is bound to have a broad and promising future. With respect to signals, it is not surprising that under a DC voltage, a diesel wall jet generated by an SDBI actuator will cease in less than 10 s. This is because in diesel oils with a conductivity of 10^{-9} S/m, more injected charges accumulate on the dielectric substrate at a higher rate, which greatly reduces the electric field around the electrode and rapidly slows down the interfacial electrochemical reaction rate. However, under a DC voltage, a silicone wall jet with a lower conductivity (10^{-13} S/m) leads to a weaker charge accumulation, which allows a nonstop flow along the surface to last for hours. An unanticipated observation is that, as opposed to all usual cases (where the direction of the jet is independent of the voltage polarity and remains away from the active electrode), the silicone wall jet possesses a reverse flow direction (toward the electrode) in the first 3 min of negative polarity. This provides strong phenomenological support for the preexistence of heterocharges (positive charges) near the interface at negative polarity voltages. Thus, the following hypothesis appears: if a bi-polar pulsed DC signal of the appropriate period is applied, then a bidirectional silicon flow is expected.

II. Theoretical Interpretation of the Interface

The polarity-dependent flow direction in silicone oil observed in the previous study is supposed to be associated with the attraction or repulsion of accumulated charges on the

Manuscript received July 28, 2022.This work was supported by National Natural Science Foundation of China (Grant No. 51907118). *(Corresponding author: Zelu Yan).*

Zelu Yan is with the Logistics Engineering College, Shanghai Maritime University, Shanghai 201306, China (e-mail: zlyan@shmtu.edu.cn).

Christophe Louste and Philippe Traoré are with the Institut PPRIME, Université de Poitiers-ISAE-ENSMA, 86962, Futuroscope Chasseneuil, France(e-mail:christophe.louste@univ-poitiers.fr, philippe.traore@univ-poitiers.fr).

Roberto Sosa is with the Laboratorio de Fluidodinámica, Universidad de Buenos Aires, CONICET, C1063ACV, Buenos Aires, Argentina (e-mail: rsosa@fi.uba.ar).

Color versions of one or more of the figures in this article are available online at http://ieeexplore.ieee.org

surface by the electrode. This underlines the plausibility of the assumption that there should be an initial charge distribution at the dielectric interface. It is obvious that because of the low conductivity of silicone oil, there exists a large relaxation time (229.3 s) associated with the electrical double layer (EDL) as well as a nonnegligible Debye charge layer (240 μm). Such a charge phenomenon provides favorable conditions for the process of interfacial charge formation. In this section, we provide a physical explanation of the initial charge formation mechanism at the dielectric solid/liquid interface before developing a theoretical model of silicone EHD wall jets.

Undoubtedly, there is an EDL in contact with the phase boundary at any interface between the two phases [5]. To date, no studies have investigated the charge formation characteristics of the polymethyl methacrylate (PMMA) /silicone oil interface, which has an EDL structure different from that of the metal/liquid interface. Recently, Wang proposed a two-step formation process of an EDL in an insulating solid film/liquid contact electrification (CE), which was verified experimentally [6]. The first step involves electron transfer between solid/liquid due to the repulsive effect of the overlapped electron cloud at the first contact with the virginal solid surface (1 out of 3×10^4 surface atoms may participate in the transfer). This step occurs even between polytetrafluoroethylene (PTFE) and ion-free transformer oil (#25 TOMA) [7]. Then, a second step refers to the redistribution of ions by ion transfer or specific adsorption associated with EDL formation [8]. According to this mechanism, we should first clarify the sign of the charged surface.

Nakajima studied the electrification properties of various insulator/silicone oil interfaces and found in experiments that by streaming electrification, PTFE is positively charged, whereas silicone oil is negatively charged [9]. The author suggested an interpretation of the electronic state between PTFE/silicone oil based on the Duke model. Note that Duke gave a description of polymer/polymer contact charge exchange, which is used to correctly predict the sign or magnitude order of contact charge exchange [10]. According to this view, both PTFE and silicone oil are considered to be donors and acceptors in the form of a Gaussian distribution. The electronic energy (equivalent work function) is located at the center of the distribution curves of the donor and the acceptor. Electrons move from PTFE with a small work function (6.71 eV) to silicone oil with a large work function (greater than 6.71 eV). As a result, the dielectric layer providing electrons becomes positively charged.

It was demonstrated that silicone oil droplets with higher charge density lead to an increased probability of their deposition on the substrate surface due to electrostatic attraction [11]. Likewise, a compound droplet with silicone oil can still leave a small residue on the fiber even after centrifugal detachment or application of a magnetic field for separation [12,13]. The physical and chemical properties of silicone oil adherence to PMMA were investigated in [14]. The results strongly suggest that the remaining silicone oil covers 12% of the PMMA lens surface even after cleaning with n-pentane. More precisely, the water vapor permeability of silicone oils is 52 times higher than that of mineral oils with comparable viscosity, resulting in a higher solubility of water in the silicone oil [15]. Water in silicone oil can react with siloxane molecules to produce different kinds of silanol [16], and the carbonyl group of PMMA tends to form hydrogen bonds with these surface silanol groups [17], thereby supporting the hypothesis of chemical bonds at the PMMA/silicone oil interface in the adsorption model. Referring to the theoretical models of adsorption and corrosion [18], the dissociated negative ions of impurities, despite the very low conductivity in our case, tend to adsorb at specific sites of the PMMA walls and form chemical bonds with the ionic species of PMMA. The Stern layer of the EDL [from the metal to the outer Helmholtz plane (OHP)] is composed of these negative ions, while the diffuse layer of the EDL consists of excess positive charges in the silicone oil. In summary, it is deduced from the electron transfer mechanism [8] that the virgin surface of PMMA is positively charged at the initial contact with silicone oil. Then, the negative ions originating from CE and dissociation of impurities move to the PMMA wall by preferential adsorption to form the Stern layer, allowing the positive charges in the diffuse layer to engage in the subsequent flow convection.

In accordance with the Boltzmann distribution model of the interfacial charge [18], 95% of the positive charges are distributed between the Stern layer and a distance equal to $3\delta_0$, with δ_0 being the Debye length (diffuse layer thickness). Tests on the near-wall space charge density of various polymer materials/transformer oils demonstrated a constant ratio of $|\rho_{w0}/\sigma_0|$ [19]. Thus, in our case, ρ_{w0} yields 10^{-4} C/m^3 under the condition that $\sigma_0=1\times10^{-13}$ S/m. Then, the space charge concentration c_{w0} (mol/m^3) in the near-wall area for a fully developed EDL is expressed as [20]

$$c_{w0}(x)=\left(\frac{\rho_{w0}}{Fz_p}\right)\frac{\cosh\left((a-x)/\delta_0\right)}{\cosh\left(a/\delta_0\right)} \tag{1}$$

where F(C/mol) is the Faraday constant, |z|=1 is the ionic valence. a =60 mm is the width between the PMMA wall and the boundary, and x is the normal coordinate away from the wall. Accordingly, the negative surface charge density ρ_s(C/m^2) at the Stern layer, which is set to be equal in charge to the integral of volume density of positive charges near the interface over the distance x, can be expressed in theory as $\rho_{s0}=-\rho_{w0}\delta_0$. In short, we can no longer avoid the physicochemical processes that occur at the microscopic interface if we seek a deeper understanding of the charge behavior associated with EHD phenomena. Underpinned by the latest scientific findings on the mechanism of liquid-solid CE and the formation of EDL, the present research provides new insights into the combination of interfacial specific adsorption model and electroconvective flow model, which allows for a physical interpretation of the observed bidirectional silicone flow induced by the SDBI actuator.

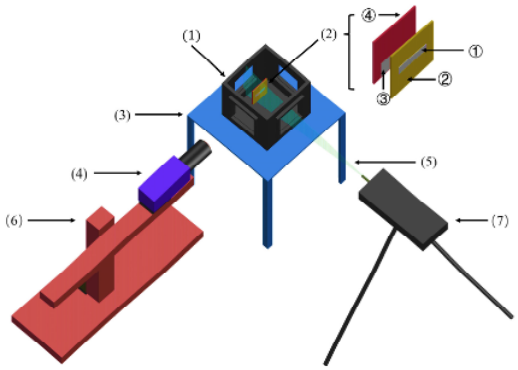

Fig. 1. Diagram of experimental facility: (1) liquid container with dimensions of 300×300×300 mm^3, (2) SDBI actuator with area of 20×60 mm^2 composed of ① active electrode, ② dielectric layer with thickness of 3 mm, ③ grounded electrode with area of 40×60 mm^2, ④ epoxy resin layer, (3) rotatable container holder, (4) CCD digital camera with spatial resolution of 2048×2048 pixels, (5) laser sheet, (6) camera displacement system, (7) laser Quantel Twins CFR with wavelength of 532 nm and power of 120 mJ at 4 Hz

III. Methodology

A. Experimental Techniques

As shown in Fig. 1, the experimental apparatus is composed of a plastic container (1) filled with silicone oil, an SDBI actuator (2), and a particle image velocimetry (PIV) system (4)-(7). The SDBI actuator consists of two planar electrodes: one blade electrode ① made up of stainless steel is exposed to the liquid, and one grounded strip ③ is buried between the PMMA layer ② and the epoxy resin layer ④. The detailed dimensions are labeled in Fig. 2. Signals with different voltage amplitudes, frequencies, duty cycles and waveforms, generated by the signal generator and amplified by TREK (±20 mA, ±20 kHz, 400 V/μs), largely affect the structure of the EHD jet. The vertically placed SDBI actuator is illuminated by the laser sheet (5). The 2D flow fields are captured by the camera LaVision, which is arranged perpendicular to the laser sheet with the help of tracer particles (diameter of 0.5 μm and concentration of 0.01 g/L). Using the phase analysis method, the time-averaged velocity field is recorded for 20 phases per signal period, and each phase velocity field is calculated from 200 instantaneous PIV measurements. Note that in our experiment, the minimum distance from the tip of the active electrode to the grounded electrode is 10.4 mm, resulting in an extreme mean electric field of 30 kV/10.4 mm ≈ 2.88×10^6 V/m. This value is much smaller than the mean field strength of 2.1×10^7 V/m corresponding to the breakdown voltage of silicone oil measured in a triple junction model which is highly similar to our SDBI structure [21]. In addition, no bubble generation was observed at the electrode tip during the experiment, and no tree-shaped streamer appeared in the raw PIV images before post-processing, ensuring that the electric field range of our experiment falls safely within that of the EHD phenomena. Consequently, the silicone oil is able to withstand the high voltages applied in this study without almost any degradation in dielectric properties.

B. Simulation model

The set of EHD equations depicting the electroconvective silicone flow can be given in the form [22]

$$\boldsymbol{E} = -\nabla\varphi \tag{2}$$

$$\nabla\cdot(\varepsilon_0\varepsilon_{rl}\boldsymbol{E}) = q \tag{3}$$

$$q = F\left(z_p c_p + z_n c_n\right) \tag{4}$$

$$\frac{\partial c_p}{\partial t} + \nabla\cdot\left(\boldsymbol{N_p}\right) = S \tag{5}$$

$$\frac{\partial c_n}{\partial t} + \nabla\cdot\left(\boldsymbol{N_p}\right) = S \tag{6}$$

$$\boldsymbol{N_p} = \kappa_p c_p \boldsymbol{E} - D_p\nabla c_p + c_p\boldsymbol{u} \tag{7}$$

$$\boldsymbol{N_n} = \kappa_n c_n \boldsymbol{E} - D_n\nabla c_n + c_n\boldsymbol{u} \tag{8}$$

$$\gamma\frac{\partial\boldsymbol{u}}{\partial t} + \gamma(\boldsymbol{u}\cdot\nabla)\boldsymbol{u} = -\nabla p + \mu\Delta\boldsymbol{u} + q\boldsymbol{E} \tag{9}$$

$$\nabla\cdot\boldsymbol{u} = 0 \tag{10}$$

where $\boldsymbol{E}$(V/m) is the electric field, φ(V) is the electric potential, ε_{rl}=2.59 is the permittivity of silicone oil, q(C/m^3) is the volume charge density, c(mol/m^3) is the ion concentration, and the subscript p stands for positive charge and n for negative charge. $\boldsymbol{N}$(mol/(m^2·s)) is the ion flux corresponding to the EHD current density given by the Nernst-Plank equations. For a silicone oil with kinematic viscosity μ=4.55×10^{-3} Pa s, we choose the ion mobility κ_p=1×10^{-9} m^2/(V s) and κ_n=5×10^{-8} m^2/(V s) reported by Holroyd, which seems to better follow the slope of Walden's rule [23]. The diffusion coefficient D=1×10^{-7} m^2/s is valid for simulation [22]. The mass density is γ=910 kg/m^3, and u(m/s) is the velocity. S is the source function describing the generated charges based on the Wien effect for the near-electrode region in a precise model.

$$S = \frac{\sigma_0^2}{F\varepsilon_0\varepsilon_{rl}\left(z_p b_p + z_n b_n\right)}H(w) - \frac{F\left(z_p b_p + z_n b_n\right)}{\varepsilon_0\varepsilon_{rl}}c_p c_n \tag{11}$$

$$H(w) = \frac{I_1(4w)}{2w} \tag{12}$$

$$w = \frac{e}{2k_B T}\sqrt{\frac{eE}{4\pi\varepsilon_0\varepsilon_{rl}}} \tag{13}$$

where the conductivity σ_0=1×10^{-13} S/m, $H(w)$ is the Onsager function, and I_1 is the modified Bessel function of the first kind and order 1. w is the ratio of the Bjerrum distance to the Onsager distance [24]. The grounded electrode embedded in the dielectric layer is not in contact with the silicone oil and therefore does not participate in charge generation and disappearance. In contrast, charge injection and discharge are defined as boundary conditions of the active electrode [24,25].

$$N_{inj,p} = \left(\frac{en}{Fl_H}\right)\left(\frac{\alpha_{ox}^0}{\alpha_{rd}^0}\right)\left(\frac{\exp(-e^2/16\pi\varepsilon_0\varepsilon_{rl}l_H k_B T)}{wK_1(w)}\right)\kappa_p E \tag{14}$$

$$N_{loss,n} = \boldsymbol{n}\cdot(b_n c_n\boldsymbol{E} - D_n\nabla c_n) \tag{15}$$

where n(1/m^2) is the concentration of ion pairs on the electrode surface, and the length of the Stern layer l_H is set to 5 nm [24]. $\alpha_{ox}^0/\alpha_{rd}^0$ is the ratio of the oxidation constant to the reduction

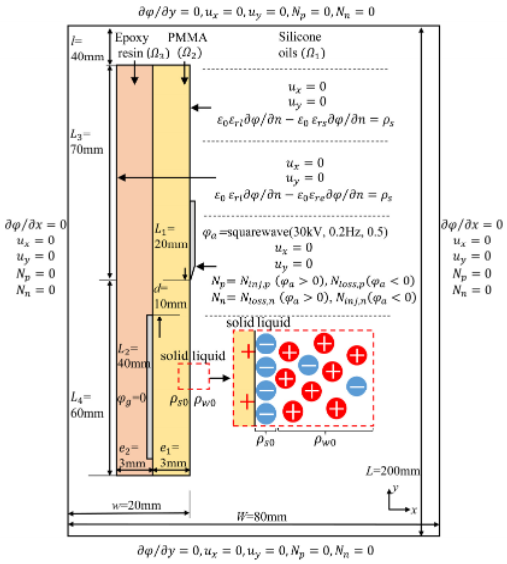

Fig. 2. Schematic representation of computational domain, boundary conditions, and physical-chemical adsorption model at interface (not to scale).

constant. K_1 denotes the modified Bessel function of the second kind and order 1. $\boldsymbol{n}$ is the unit vector normal to the electrode surface. Indeed, by phenomenologically matching the time-averaged velocity in the simulation with that in the experiment [22], we can derive $n\alpha_{ox}^0/\alpha_{rd}^0$=6043(1/m^2) as the intrinsic characteristic of the solid/liquid interface [24]. Note that (14) and (15) characterize the injection of positive charges and the discharge of negative charges during positive polarity, respectively, and vice versa for the negative polarity half-cycle.

Fig. 2 shows the boundary conditions with a simulation domain inclusive of the working fluid Ω_1, substrate region Ω_2 and encapsulated layer Ω_3. Ω_1 is controlled by both electric and flow field equations, while Ω_2 and Ω_3 are solely governed by electric field equations. The simulations are conducted from the moment the fluid is at rest, the equilibrium ion concentration without an electric field is c_{p0}=c_{n0}=2.03×10^{-11} mol/m^3, the constant charge density ρ_{s0} at the Stern layer is derived as -2.39×10^{-8} C/m^2 using the expression in Section II, while the initial charge distribution in the diffuse layer obeys (1) with ρ_{w0}=1×10^{-4} C/m^3. Note that these initial charge values on the EDL will play a vital role in the subsequent fluid motion in our silicone case. Once the electric field begins to act on the fluid, the charges in the EDL in the liquid phase will be subjected to migration, convection and diffusion.

A software package based on the finite element method was successfully employed to solve the entire EHD electroconvective problem [26,27]. For the critical equations such as electrochemical injection, Wien effect, and charge accumulation that the software cannot automatically provide the corresponding descriptions for the SDBI geometry, we defined custom models using equation-based modeling and implemented them in the entire interface. At the PMMA/silicone oil interface, discretization is carried out along the slip-free boundary by using layered quadrilateral meshes in the normal direction. In the bulk, unstructured triangular meshes are used. The minimum grid size of 10^{-6} m ensures sufficient resolution of the high-density space charge region, which extends to $3\delta_0$≈720 μm. Then, the propagation of the EHD wall jet accompanied by charge convection and accumulation can be well resolved. The backward differentiation formula and the time-dependent solver are adopted. At each time step, the relative error is below 0.1%. The mesh refinement tests are iterated until the change in the converged solution between two tests is less than 0.5%.

IV. Results and Discussion

A. Flow structure

In this study, the order of magnitude of power consumption is about 0.1 mW/m in the silicone oil with low conductivity (characterized by linear density for this 2D model), verifying the low energy consumption of the EHD technology. Under a square wave voltage with an amplitude of 30 kV, frequency of 0.2 Hz, and duty cycle of 50%, velocity fields generated by the SDBI actuator at t^*=0.5 and t^*=0.7 are shown in Fig. 3 and Fig. 4, respectively. t^* is defined as t/T, where T stands for the signal period. The signal is specified to provide a positive polarity at t^*=0~0.5 and a negative polarity at t^*=0.5~1. In the experiment, the interval between two successive phases is equal to Δt^*=0.05 for the entire cycle. The velocity results based on the charge generation and adsorption model in the simulation [see Fig. 3(b) and Fig. 4(b)] are essentially consistent with the experimental findings [see Fig. 3(a) and Fig. 4(a)]. This allows us to analyze the flow field properties from the intrinsic perspective of charge interactions in the following.

When the positive polarity is applied to the SDBI actuator, the injected charges near the tip are repelled by the electrode, leading to the development of an electroconvective silicone jet downstream along the wall. The silicone jet with a lower conductivity acquires only 10% of the velocity maximum compared to the wall jet in diesel oil at t^*=0.5 (approximately 0.032 m/s in the silicone case) but obtains a wider half-width and a more evident detachment characteristic away from the wall (which is probably attributed to homocharge interaction between preexisting and injected charges). The counterclockwise rotating vortex V_1 formed near the electrode tip is convected by the jet and gradually expands, with the vortex center located at (10 mm, -15 mm) when t^*=0.5.

However, at the negative polarity half-cycle, opposite to the direction of the diesel jet that always flows downward, Fig. 4 exhibits a clockwise rotating vortex V_2 attracted upward by the electrode near (5 mm, 2.5 mm). This reverse flow in the negative half-cycle is likely to be associated with the positive surface charge layer accumulated in the first half-cycle. The absence of a vortex V_3 in Fig. 4(a) is due to the smoothing effect of the time-averaged calculation of the PIV instantaneous velocity fields at the same phase. In the region of y <-10 mm,

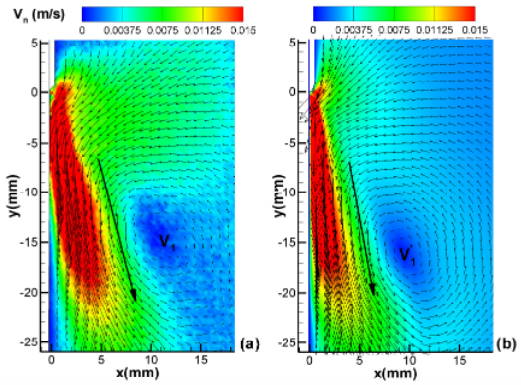

Fig. 3. Velocity modulus and vectors of flow field obtained by (a) PIV measurement and (b) simulation at phase t^*=0.5 under square wave signal with U_m=30kV, f=0.2 Hz.

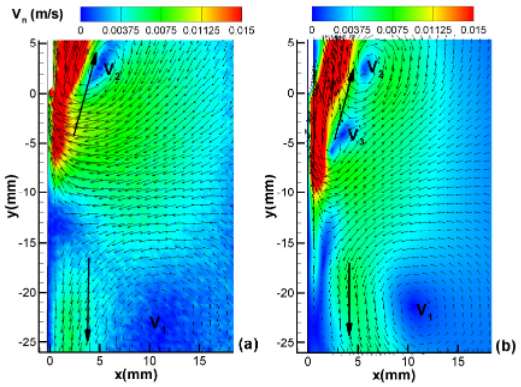

Fig. 4. Velocity modulus and vectors of flow field obtained by (a) PIV measurement and (b) simulation at phase t^*=0.7 under square wave signal with U_m=30kV, f=0.2 Hz.

the wall jet generated at the positive polarity half-cycle is still moving inertially downstream and is accompanied by the vortex V_1.

B. Velocity profile and turbulence quantity

In a traditional 2D plane wall jet, the time-averaged velocity profile and turbulence quantity are used to identify the boundary layer and characterize the pulsation level [28]. Therefore, it is of great importance to compare these features between silicone EHD wall jets and classical plane wall jets. For a classical wall jet, the time-averaged velocity profile at the outer scale will reach a self-similar state in the fully developed region, i.e., there is a perfect collapse of the velocity profile data for these cross sections [28]. Then, for a silicone EHD wall jet, we find that cross sections with self-similarity properties appear in the range from y/e=1 to y/e=3, where e=3 mm is the layer thickness.

Fig. 5 shows the velocity profiles in the self-similar region for both simulation and experiment. The simulation data fit well with the experimental data from y/e=1 to y/e=3. A typical parameter describing a classical wall jet is $x_m/x_{1/2}$, indicating the ratio of the maximum streamwise velocity point away from the wall to the jet's half-width. For a plane wall jet, $x_m/x_{1/2}$ varies from 0.13 to 0.17 in different studies [28], yet in our case, $x_m/x_{1/2}$ yields a much larger value of approximately 0.35. This thicker inner layer of the silicone wall jet might be attributed to two factors: liquid viscosity and charge distribution near the wall. Specifically, the higher kinematic viscosity of silicone oil compared to a conventional water jet (5cst versus 1cst) makes it more difficult for the silicone jet to move forward along the surface, so the jet tends to separate from the wall. Moreover, the charge interaction near the wall under the electric field intensifies the flow convection, increasing the possibility for the jet to "take off" from the wall.

We now verify whether the turbulence intensity of the silicone wall jet is as high as the analysis we have just done. In Fig. 6, with reference to the conventional wall jet, we use the mean-square perturbation of the streamwise velocity $\overline{v_y'^2}$, normalized by the square of the streamwise velocity maximum

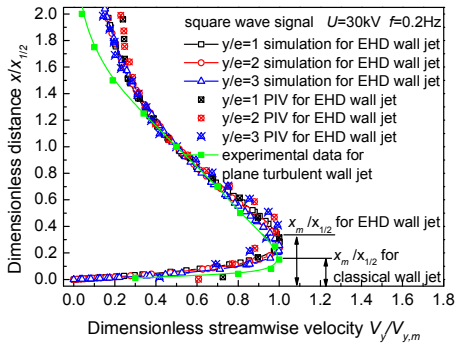

Fig. 5. Streamwise velocity profiles in self-similar region from y/e=1,2,3 scaled in dimensionless form with outer parameters of $V_{y,m}$ and $x_{1/2}$ at instant t^*=0.5: hollow symbols representing simulation, hollow symbols filled with × indicating PIV measurements and solid symbols denoting classical plane wall jet.

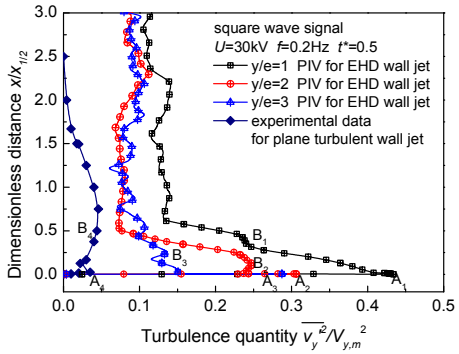

Fig. 6. Turbulence quantity profiles in self-similar region from y/e=1,2,3 scaled in dimensionless form with outer parameters of $V_{y,m}^2$ and $x_{1/2}$ at instant t^*=0.5: hollow symbols filled with × indicating PIV measurements and solid symbols denoting classical plane wall jet.

$V_{y,m}^2$, to assess the pulsation characteristic of the jet [29]. To facilitate comparison, the double-peaked profile of the turbulence quantity curve of the plane wall jet in the self-similar region is also plotted in Fig. 6 (see solid symbols). Note that all curves of the cross sections in the self-similar region overlap each other for the classical jet, with a near-wall peak A_4 equal to 0.03 and an outer peak B_4 (located at approximately $x/x_{1/2}$≈0.7) equal to 0.04. Nevertheless, although the same cross sections of the self-similar region as in Fig. 5 are selected, the turbulence quantity profiles of these cross sections are not superimposed as expected for the silicone jet. This implies that the turbulence characteristic near the interface is influenced by the coupling of mechanical and electric field forces rather than only mechanical force. Among the sections in Fig. 6, the highest near-wall peak appears at y/e=1 with A_1≈0.44, and its outer peak B_1≈0.23 is located at $x/x_{1/2}$≈0.5. It can be inferred that the interaction between the injected charges at the electrode and the accumulated charges near the substrate is the main contributor to this higher turbulence quantity. The shorter the section-to-electrode distance, the stronger the charge interaction subjected to the electric field, and therefore the more intense the turbulence level possessed by the EHD wall jet.

C. Space charge density and vortex distribution

The aforementioned analysis suggests that the flow field at the wall has a strong interaction with the electric field. Hence, in Fig. 7 and Fig. 8, we plot the distribution of electric field, and typical coupling of the vortex and space charge at t^*=0.3 and t^*=0.9. These two moments are located in the mid-stage of the half-cycle of the square wave and possess a similar electric field distribution. In view of the small curvature of the two electrodes and their oblique arrangement, the maximum value of the electric field is located at the tip of the electrode reaching 10^7 V/m. The electric field radiates outward from the tip of the electrode and decreases sharply with distance away from the electrode. Despite the continuous distribution of the tangential component of the electric field E_t, the normal component E_n affected by the accumulated space charges results in a discontinuity of the resultant field $\boldsymbol{E}$ at the boundary. The main space charges in Fig. 7 are confined to a limited rectangular area with a width of approximately 2 mm. It can be seen that accumulated charges in this positive half-cycle develop downstream with the flow field, establishing a thicker zone 2. In the far-field region, initial charges caused by CE are retained in zone 1 and are not yet affected by the charges that are propagating from the upstream field. At the junction of zone a and b, where y=-20 mm, the injected charge front is observed to have a half mushroom-shaped charge head. Referring to the full mushroom-shaped charge head of the free EHD jet reported in [30], it is reasonable that the injected charge front in our case retains only half of it with the wall as the axis of symmetry.

With the Q-criterion, we are able to detect the vortex in the wall-bounded free shear flows [31]. The shear-induced vortices B and C are easily identified in the magnified image in Fig. 7 (a), which shows the vortex centers corresponding to the

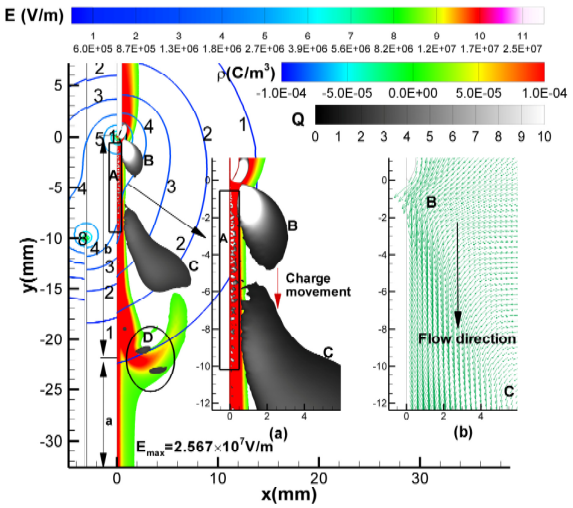

Fig. 7. Distribution of electric field (large rainbow), space charge (small rainbow) and vortex (grayscale) near dielectric interface at phase t^*=0.3: (a) enlarged view near electrode and (b) vector map of corresponding flow field.

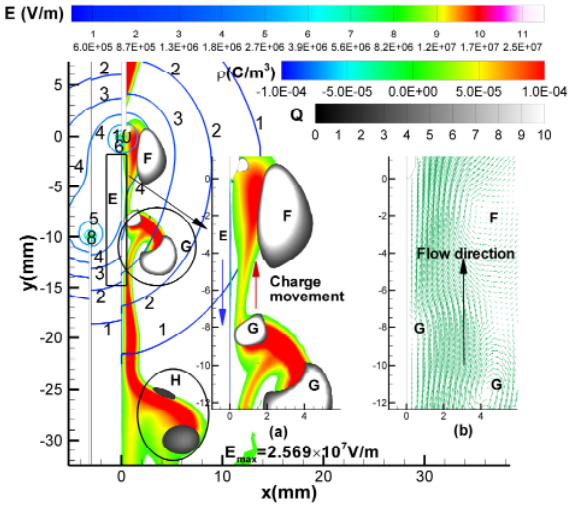

Fig. 8. Distribution of electric field (large rainbow), space charge (small rainbow) and vortex (grayscale) near dielectric interface at phase t^*=0.9: (a) enlarged view near electrode and (b) vector map of corresponding flow field.

velocity field in Fig. 7(b). Similar to the free jet, the vortex pair D is formed on both sides of the charge column that has already detached from the wall. The Q-criterion measures the extent to which the vorticity magnitude prevails over the shear strain rate, and it has already been applied to EHD flows [1]. This method has an advantage in detecting vortex structures near the wall,

whereas the commonly used vorticity magnitude criterion may confuse the vortex structures with the boundary layer and can detect only one continuous vortex column along the wall. In Fig. 7, a vortex chain distributed in the accumulated charge region A is clearly observed using the Q-criterion, and these smaller vortex structures implying stronger velocity pulsations

are verified by their high turbulence quantities in the same region ranging from y/e=1 to y/e=3 in Fig. 6.

Fig. 8 shows that the charge distribution behavior in the negative half-cycle is more complex than that of the positive polarity. It can be seen that positive charges accumulated during the first half-cycle are attracted by the electrode and migrate upward in the outer layer (see red arrows), while negative charges are injected downstream along a very narrow channel next to the wall in the inner layer (see region E and blue arrows). In fact, at the beginning of the negative half-cycle, the number of positive charges benefiting from accumulation in the first half-cycle is much greater than that of negative charges. These positive charges attracted by the electrode leave the wall, enter the liquid and eventually arrive at the outer surface of the electrode for neutralization. During this process, the positive charges distributed in the diffuse layer inevitably participate in upward convection, and the full mushroom-shaped head of positive charges detaches from the wall. This is accompanied on both sides by typical induced vortices (see vortex pairs G and H). However, with respect to the electrode tip, which is much closer to the wall, the negative charges injected from it are more likely to accumulate immediately on the surface, and their movement can hardly contribute to the flow convection near the wall. The unbalanced distribution range of positive and negative charges in Fig. 8 and the evidence of upward silicone flow seem to indicate that the negative polarity injection is completely suppressed.

To gain insight into this issue, Fig. 9 plots the variation in the charge density against distance in the near-wall diffuse layer during a complete square wave cycle. At the end of each half-cycle (t^*=0.5 and t^*=1), the charge density curve exhibits a peak-valley-peak profile. Taking curve 4 (t^*=0.5) as an example, in the near-electrode region, the number of charges generated by electrochemical injection and field-enhanced dissociation depends mainly on the local electric field, and these generated charges are more affected by migration than convection in this low-velocity region. This is why the charge distribution law mirrors that of the electric field, weakening sharply with increasing distance. The curve levels off and reaches a minimum (0.002 C/m^3) at -7 mm< y <-3 mm, then rises again to another peak (0.01 C/m^3) followed by a second drop at a distance away from the electrode. It appears that the combination of charge conduction and convection yields this valley-peak characteristic: normalwise migration makes it easier for charges to be deposited on the surface, while streamwise convection prevents them from accumulating on the surface. For example, charges at the valley of the curve are pushed downstream by the maximum convective intensity and thus are difficult to deposit on the surface, while near the second peak, the streamwise velocity gradually vanishes, and the charges propagating from upstream accumulate rapidly.

Regarding the temporal variation of the curve, the evolution path of the charge density in the positive half-cycle follows the sequence of curves 1→2→3→4, while that in the negative half-cycle follows the sequence of 1'→2'→3'→4'. For the

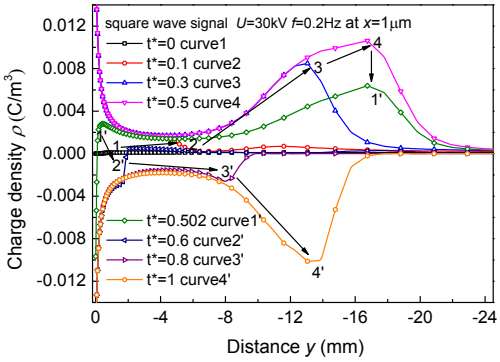

Fig. 9. Evolution of space charge density at position x=1μm with distance downstream for one complete cycle. $|\rho_{max}|$ =0.017C/m^3 obtained near electrode for both signal polarities is beyond coordinate range and thus not shown on curves.

transition of voltage polarity from positive to negative (4→1'), the reversal of charge polarity in curve 1' at the electrode tip confirms the effectiveness of the negative charge injection. The drop of its curve peak in the far field (y≈-18 mm) is probably not the result of recombination of accumulated positive charges with injected negative charges since the injected charges cannot propagate as far during polarity alternation. A reasonable deduction is that the detachment of the positive charges from the wall (see Fig. 8) lowers the charge density in the diffuse zone, and the unchanged peak position (for 4 → 1', the coordinates remain y≈-18 mm) supports the view that positive charges are moving normal to the wall (in the x direction) rather than traveling upward along the y axis. Another significant aspect is that the position of the second charge density peak at t^*=1 is slightly closer to the electrode than that of the peak at t^*=0.5, which signifies that the movement of the accumulated positive charges at the negative half-cycle more or less retards the propagation of the injected negative charges.

D. Influence of signal parameters on velocity

This section seeks to evaluate the effect of various bi-polar pulsed DC signals on the flow features of each polarity. We select the mean streamwise velocity of $\bar{V}_y$ as the evaluating index at the reference point (1.4 mm, -6.1 mm), which can reflect the flow characteristics in the core region of the silicone wall jet. $\bar{V}_y$ for each polarity is obtained by averaging all phase velocities over a half-cycle.

Fig. 10(a) shows the variation of $\bar{V}_y$ with the amplitude of the square wave voltage for each polarity. The polarity-dependent flow direction is visible, and the velocity increases with the applied voltage. The velocity under positive polarity has a greater growth rate, and at 30 kV, the velocity of 0.03 m/s tends to reach an asymptotic value. In contrast, the velocity under negative polarity has a slower rate of increase despite linear growth.

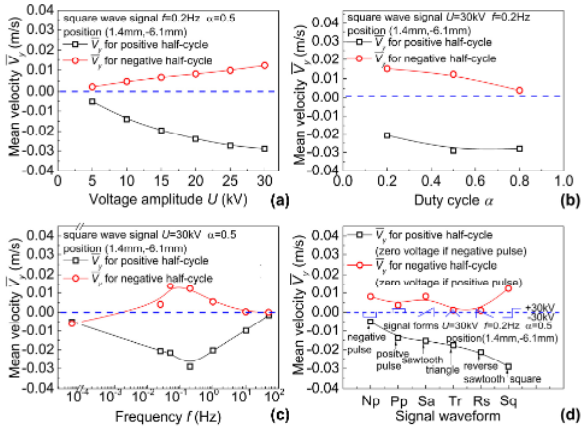

Fig. 10. Evolution of $\bar{V}_y$ at point (1.4 mm, -6.1 mm) with (a) voltage amplitude, (b) duty cycle and (c) frequency for each polarity of square wave; (d) signal forms.

Fig. 10(b) indicates the impact of the duty cycle on $\bar{V}_y$ for each polarity. Under negative polarity, as α (defined as the ratio of positive polarity duration to the total period) increases, $\bar{V}_y$ decreases significantly due to the lack of sufficient time to move upward. In contrast, for positive polarity, $\bar{V}_y$ increases with increasing α. At α=0.5, the jet reaches its maximum velocity, implying that the silicone wall jet takes less time to reach a steady state at positive polarity.

Fig. 10(c) presents the influence of the signal frequency on $\bar{V}_y$ for each polarity. The bidirectional feature of silicone wall jets is valid only when the frequency is on an order of magnitude ranging from 10^{-2} Hz to 10^{1} Hz, in which f=0.2 Hz corresponds to a jet with maximum kinetic energy. The effect of a square wave with a very low frequency can be equivalent to that of DC signals of both polarities, where the time-averaged flow field at each polarity always records a downward-flowing jet with a velocity of only 0.005 m/s despite the presence of a transient upward flow at the beginning of the negative polarity [2]. The accumulated charges on the dielectric surface under the effect of a continuous unipolar signal greatly reduces the electric field, resulting in a low velocity flow. The jet is also fairly weak when the frequency exceeds 100 Hz, which is in agreement with that of EHD flows in transformer oils [32]. First, too high a frequency represents too frequent a polarity alternation, and the flow field exhibits oscillation rather than movement. Second, the injected charges are repeatedly repelled and attracted in the near field at such a high frequency, making it difficult for them to contribute to convection.

Fig. 10(d) illustrates the effect of the different signal waveforms on $\bar{V}_y$ for each polarity. The square waveform performs best in generating a high-velocity flow field, followed by the triangular waveform types, and the pulsed types have the lowest efficiency in electrical-kinetic energy conversion. For example, in the case of a positive half-cycle (or zero voltage for negative pulse), the square wave and three triangular signals have a peak-to-peak of 60 kV compared to only 30 kV for the two pulsed signals. The stronger electric field gradient at the polarity transition results in a faster jet. Then, looking at the top four signals with the highest flow velocity of all signals, the slope at the moment of transition from negative to positive (the rising edge) for square and reverse sawtooth waves (theoretically infinite) is much greater than that of 24 kV/s for triangular waves and 12 kV/s for sawtooth waves, allowing the first two waveforms to produce a more efficient jet. Finally, regarding the top two signals, the great slope (falling edge) of the square wave allows the accumulated positive charges to dissipate more quickly in the shorter time after the polarity change from positive to negative. This facilitates the establishment of a stronger electric field in the following positive half-cycle. In contrast, the slope of -12 kV/s makes it difficult for the reverse sawtooth to remove the accumulated charges rapidly. Hence, the square wave is more advantageous. Moreover, bidirectional flow is still observed, although the pulsed signal possesses zero voltage for the half-cycle duration. In fact, when the voltage goes to zero, charge discharge occurs at the active electrode, which causes the flow direction in the first polarity half-cycle to reverse after the inertia disappears.

V. Conclusion

This study provided a systematic description of the charge distribution and bidirectional flow behavior of silicone flow generated by an SDBI actuator under bi-polar pulsed DC signals by simulation and experiment. Based on a theoretical explanation of the preexisting positive charges at the PMMA/silicone oil interface, an EHD model considering the charge accumulation effect was established, and the simulation results were in agreement with those observed in PIV measurements for bidirectional flow. The maximum downward velocity of 0.03 m/s for the positive half-cycle equaled twice the upward velocity for the negative half-cycle. The thicker half-width of the silicone wall jet compared to that of a classical wall jet was due to the strong interaction between injected charges and accumulated charges in the near-surface region. Correspondingly, the turbulence quality, which was 10 times greater than that of the classical wall jet, also confirmed the intense charge activities. More essentially, we shed light on the silicone electroconvective phenomenon through the nature of charge-vortex coupling. During the positive polarity half-cycle, the injected charges repel the preexisting positive charges, moving downstream with the generated vortex. At negative polarity, the accumulated positive charges enter the diffuse layer and more far-reaching regions, where they are rapidly committed to upward convection. Although the injection strength remains unchanged, the negative charges move downstream along the surface from a very thin finite channel, leaving a misleading intuitive impression that charge injection is entirely suppressed at negative polarity. Studies of the effect of signal parameters on velocity showed that the bidirectional silicone flow is only valid for signals in a certain frequency range, and among all waveforms, the square wave is the most effective. Considering the good response of velocity to

signal parameters, the results of this work can be employed for flexible and controlled manipulation of silicone fluids for potential microfluidic applications in biology, medicine, and microelectronics. In future work, the interfacial phenomena induced by silicone oils with different properties and other dielectric substances in the SDBI actuator will be investigated.

REFERENCES

[1] C. Louste, M. Daaboul, and H. Romat, "A study of vortex shedding induced by dielectric barrier injection," *J. Electrostat*., vol. 67, pp. 348-353, May, 2009, doi: 10.1016/j.elstat.2009.02.007.

[2] C. Louste, Z.Yan, P.Traoré and R.Sosa, "Electroconvective flow induced by dielectric barrier injection in silicone oil," *J. Electrostat*., vol. 71, pp. 504–508, Jun., 2013, doi: 10.1016/j.elstat.2012.12.037.

[3] J. Hong, Y. Kim, and D. Won, "Three-dimensional digital microfluidic manipulation of droplets in oil medium," *Sci Rep*, vol. 5, p. 10685, Jun., 2015, doi: 10.1038/srep10685.

[4] L. Yang et al., "Flow distribution control in meso scale via electrohydrodynamic conduction pumping," *IEEE Trans. Ind. Appl*., vol. 53, no. 2, pp. 1431-1438, Mar.-Apr., 2017, 10.1109/TIA.2016.2626358.

[5] J. O. M. Bockris, K. N. Reddy, and M. Gamboa-Aldeco, *Modern Electrochemistry 2A Fundamentals of Electrodics*. Springer, Boston, MA, 2000.

[6] S. Lin, X. Liang, A. Wang, and Z. Wang, "Quantifying electron-transfer in liquid-solid contact electrification and the formation of electric double-layer," *Nature Communications*, vol. 11, pp. 399, Jan., 2020, doi: 10.1038/s41467-019-14278-9.

[7] J. Nie et al., "Probing contact electrification induced electron and ion transfers at a liquid-solid interface," *Advanced Materials*, vol. 32, Nov., 2019, doi: 10.1002/adma.201905696.

[8] Z. L. Wang and A. C. Wang, "On the origin of contact-electrification," *Materials Today*, vol. 30, pp. 34-51, Nov., 2019, doi: 10.1016/j.mattod.2019.05.016.

[9] A. Nakajima, H. Miyahara, T. Ishikawa, J. Wada, and Y. Satoru, "Streaming electrification characteristics of silicone oil," *IEEE Trans. Dielectr. Electr. Insul*., vol. 15, pp. 519-526, May, 2008, doi: 10.1109/TDEI.2008.4483472.

[10] C. Duke and T. Fabish, "Contact electrification of polymers: A quantitative model," *J. Appl. Phys*., vol. 49, pp. 315-321, Feb., 1978, doi: 10.1063/1.324388.

[11] H. Nazir et al., "Multilayered silicone oil droplets of narrow size distribution: Preparation and improved deposition on hair," *Colloids Surf. B*, vol.100, pp.42-49, Dec., 2012, doi: 10.1016/j.colsurfb.2012.05.018.

[12] H. J. Holweger, M. Jamali, and H. V. Tafreshi, "Centrifugal detachment of compound droplets from fibers," *Langmuir*, vol. 37, no. 2, pp. 928-938, Jan., 2021, doi: 10.1021/acs.langmuir.0c03317.

[13] N. M. Farhan and H. V. Tafreshi, "Using magnetic field to measure detachment force between a nonmagnetic droplet and fibers," *Langmuir*, vol. 35, no. 25, pp. 8490-8499, Jun., 2019, doi: 10.1021/acs.langmuir.9b01313.

[14] C. Kim, C.-K. Joo, H. J. Chun, B. Yoo, D. Noh, and Y. Shim, "Instrumental studies on silicone oil adsorption to the surface of intraocular lenses," *Applied Surface Science*, vol. 262, pp. 146–152, Dec., 2012, doi: 10.1016/j.apsusc.2012.03.113.

[15] M. Harz and M. Knoche, "Droplet sizing using silicone oils," *Crop Prot*., vol. 20, no. 6, pp. 489-498, Jul., 2001, doi: 10.1016/S0261-2194(01)00014-X.

[16] J. P. Crine, R. Grob, J. Casanovas, and H. Garbay, "Influence of water and silanol contents on some electrical properties of silicone oil," *IEEE Trans. Electr. Insul*, vol. EI-21, no.2, pp. 233-237, May, 1986, doi: 10.1109/TEI.1986.348951.

[17] E. Enriquez, H. Schneider, and S. Granick, "PMMA adsorption over previously adsorbed PS studied by polarized FTIR - ATR," *Journal of Polymer Science Part B: Polymer Physics*, vol. 33, pp. 2429-2437, Dec., 1995, doi: 10.1002/polb.1995.090331714.

[18] P. D. S. Clermont, T. Paillat, and P. Leblanc, "Numerical study on the impact of a temperature step on the electrical double layer," *J. Electrostat*., vol. 95, pp. 13-23, Oct., 2018, doi: 10.1016/j.elstat.2018.07.006.

[19] J. Vazquez-Garcia, J. Rivenc, A. Agneray, T. Paillat and G. Touchard, "A critical approach to measure streaming current: case of fuels flowing through conductive and insulating polymer pipes," *IEEE Trans. Ind. Appl*., vol. 41, no. 5, pp. 1335-1342, Sep.-Oct., 2005, doi: 10.1109/TIA.2005.853378.

[20] J. M. Cabaleiro, T. Paillat, O. Moreau, and G. Touchard, "Flow electrification of dielectric liquids in insulating channels: Limits to the application of the classical wall current expression," *J. Electrostat*., vol. 66, no. 1, pp. 79-83, Jan., 2008, doi: 10.1016/j.elstat.2007.08.003.

[21] J. Wada et al., "Surface Breakdown Characteristics of Silicone Oil for Electric Power Apparatus," *IEEE Trans. Dielectr. Electr. Insul*., vol. 13, pp. 830-837, Sep., 2006, doi: 10.1109/TDEI.2006.1667742.

[22] V. A. Chirkov, Y. K. Stishkov, and A. A. Sitnikov, "Simulation of the integral electric current characteristics of unsteady-state current passage through liquid dielectrics," *IEEE Trans. Dielectr. Electr. Insul*., vol. 22, no. 5, pp. 2763-2769, Oct., 2015, doi: 10.1109/TDEI.2015.005110.

[23] W. Schmidt and K. Yoshino, "Ion mobilities in mon-polar dielectric liquids: silicone oils," *IEEE Trans. Dielectr. Electr. Insul*., vol. 22, no.5, pp.2424-2427, Oct., 2015, doi: 10.1109/TDEI.2015.005036.

[24] A. Castellanos, *Electrohydrodynamics*. New York, NY, USA: Springer-Verlag Wien, 1998.

[25] S. A. Vasilkov, V. A. Chirkov, and Y. K. Stishkov, "Electrohydrodynamic flow caused by field-enhanced dissociation solely," *Phys. Fluids*, vol. 29, no. 6, pp. 063601, Jun., 2017, doi: 10.1063/1.4984837.

[26] E. Dickinson, H. Ekström, and E. Fontes, "COMSOL Multiphysics (R): Finite element software for electrochemical analysis. A mini-review," *Electrochem. Commun*, vol. 40, pp. 71–74, Mar., 2014, doi: 10.1016/j.elecom.2013.12.020.

[27] M. Becerra, H. Frid, and P. A. Vázquez, "Self-consistent modeling of laminar electrohydrodynamic plumes from ultra-sharp needles in cyclohexane," *Phys. Fluids*, vol. 29, no. 12, pp. 123605, Dec., 2017, doi: 10.1063/1.5001000.

[28] J. Eriksson, R. Karlsson, and J. Persson, "An experimental study of a two-dimensional plane turbulent wall jet," *Exp Fluids*, vol. 25, pp. 50-60, Jun., 1998, doi: 10.1007/s003480050207.

[29] G. N. Abramovich, *The Theory of Turbulent Jets*. Cambridge, MA, USA: MIT Press,1963.

[30] P. Traoré, J. Wu, C. Louste, Q. Pelletier, and L. Dascalescu, "Electrohydrodynamic plumes due to autonomous and nonautonomous charge injection by a sharp blade electrode in a dielectric liquid," *IEEE Trans. Ind. Appl.*, vol. 51, no. 3, pp. 2504-2512, May-Jun., 2015, doi: 10.1109/TIA.2014.2382763.

[31] J. Jeong and F. Hussain, "On the identification of a vortex," *J. Fluid Mech*., vol. 285, pp. 69-94, Feb., 1995, doi: 10.1017/S0022112095000462.

[32] Z. Sun, D. Sun, J. Hu, P. Traoré, H.-L. Yi, and J. Wu, "Experimental study on electrohydrodynamic flows of a dielectric liquid in a needle-plate configuration under direct/alternating current electric field," *J. Electrostat*., vol. 106, pp. 103454, Jul., 2020, doi: 10.1016/j.elstat.2020.103454.